Nano Today 38 (2021) 101145

Contents lists available at ScienceDirect

Nano Today

journal homepage: www.elsevier.com/locate/nanotoday

Precise tailoring of multiple nanostructures based on atomic layer assembly via versatile soft-templates

Guangzhou Geng[a], Wei Zhu[a], Ruhao Pan[a], Zhongshan Zhang[a], Changzhi Gu[a,b,*], Junjie Li[a,b,c,*]

[a] Beijing National Laboratory for Condensed Matter Physics, Institute of Physics, Chinese Academy of Sciences, Beijing 100190, China
[b] School of Physical Sciences, CAS Key Laboratory of Vacuum Physics, University of Chinese Academy of Sciences, Beijing 100049, China
[c] Songshan Lake Materials Laboratory, Dongguan, Guangdong 523808, China

ARTICLE INFO

Article history:
Received 4 December 2020
Received in revised form 24 February 2021
Accepted 28 March 2021
Available online xxxx

Keywords:
Multiple nanostructures
Atomic layer deposition
3D nanofabrication
Metasurface
Gas sensor

ABSTRACT

Nanodevices have higher requirements for nanofabrication in tuning the size, shape and spatial arrangement of nanostructures and their assemblies in nanoscale, however, which are often beyond the reach of conventional lithography or self-assembly techniques. In view of the above, we develop atomic layer assembled nanofabrication based on soft-templates to break through the limitations of traditional rigid-templates, having very well scalability and powerful fabrication capability for multiple solid or hollow nanostructures. Versatile soft-templates can be freely patterned at the nanoscale by mature lithographic processes, along which a precisely controlled atomic layer deposition can assemble high-aspect-ratio nanostructures with a flexible tailoring of the size, shape and spatial array, and then a dry etching process removes soft scaffolds and leaves freestanding nanostructures over large-area, rigid or soft substrates. To highlight the potentials of this fabrication strategy, the high-performance optical metasurface and ultra-sensitive H_2 gas sensor are demonstrated. This approach endows the conventional lithography and assembly techniques with new powerful functionalities and more scalability in nanofabrication, providing a simply promising route to generating complex multiple nanostructures, towards a broad application in modern nanodevices.

Introduction

Due to the unique structural advantages of the functionally periodic nanostructures, they are drawing more and more attention in photonics [1], electronic [2], piezoelectric [3,4], energy storage devices [5,6], sensing detection [7] and other applications in nanoscience. Various techniques have been used to fabricated such periodic nanostructure arrays, such as lithography [8,9], focused-ion beam [10], anodic oxidation [11,12], selective etching [13] and self-assembly [14,15], etc. But these techniques commonly have some obvious limitations in controlling the materials diversity, cross-scale sizes or irregular shapes of the resulting nanostructures, such as various metal oxides, hybrid structure, variable-diameter nanostructure, as well as multiple nanostructures, directly influencing the developments and applications of periodic nanostructures. What's more, modern nanodevices have higher requirements for nanofabrication in tuning the size, shape and spatial arrangement of nanostructures and their assemblies in nanoscale, however, which are often beyond the reach of conventional lithography or self-assembly techniques.

Recently atomic layer deposition (ALD) assisted nanofabrication has shown powerful ability and opened a new path for configuring diversiform nanostructures, based on some hard template mode mainly including silicon (Si) and anodic aluminum oxide (AAO). It is well known that ALD is a powerful thin film deposition technique that provides excellent step coverage, and a precise control of film thickness at the angstrom scale, which is due to its growth mechanism based on self-limiting surface reactions [16,17]. ALD also possesses excellent conformality due to the possibility to deposit conformal thin films on substrates of any size or shape with a high aspect ratio [18–21]. By virtue of ALD superiority, ALD assisted nanofabrication process includes ALD process filling the patterned templates and then removing the templates and finally realizing the independent nanostructures, and thus which is highly dependent on the template structures.

The templates for ALD assisted nanofabrication include rigid and soft templates. Silicon and anodic aluminum oxide (AAO) are traditionally selected as rigid-templates due to its good structural

* Corresponding author at: Beijing National Laboratory for Condensed Matter Physics, Institute of Physics, Chinese Academy of Sciences, Beijing 100190, China
E-mail addresses: czgu@iphy.ac.cn (C. Gu), jjli@iphy.ac.cn (J. Li).

https://doi.org/10.1016/j.nantod.2021.101145
1748-0132/

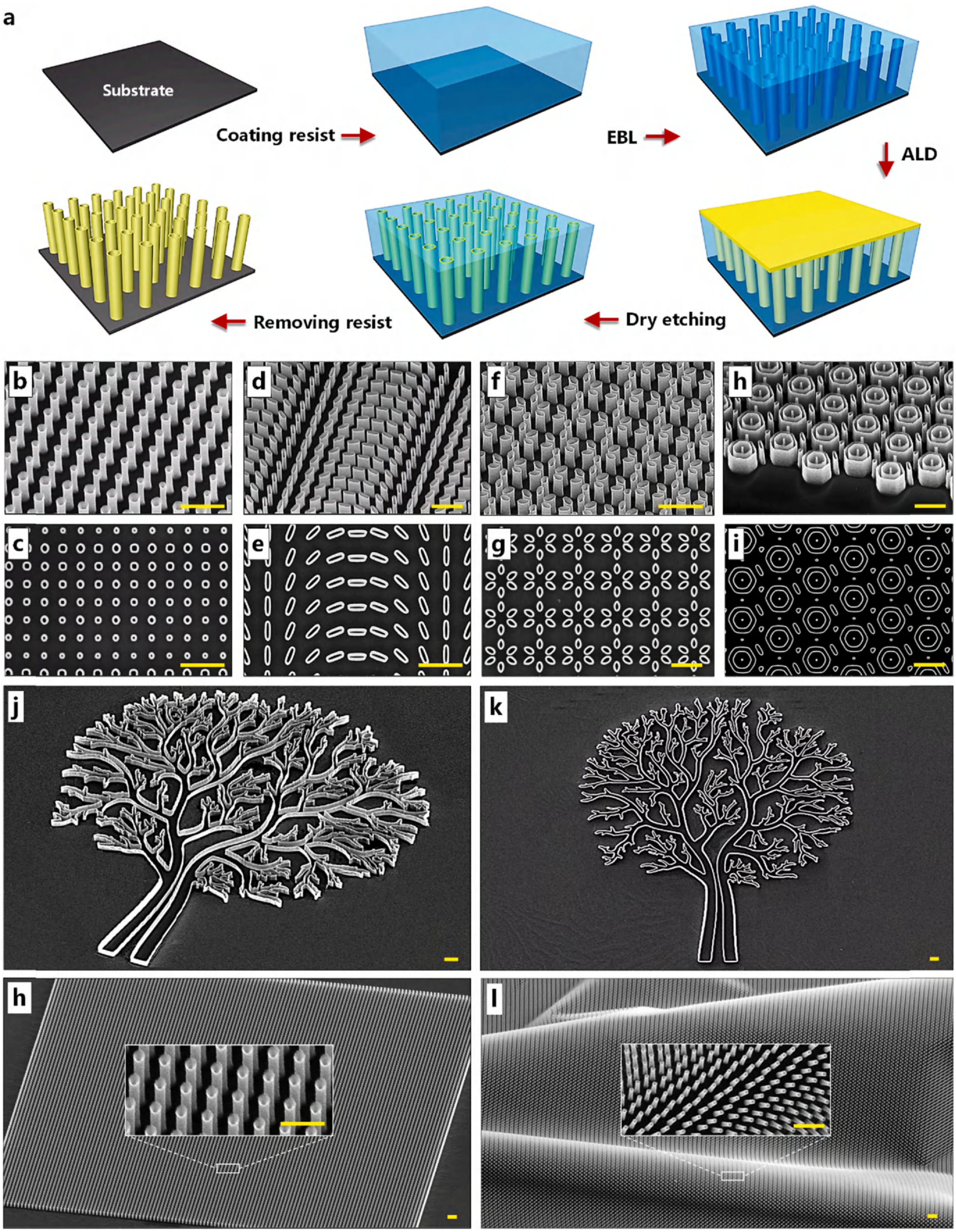

Fig. 1. (a) Schematic of ALAF process, including EBL, ALD, dry etching and removing resist. Tilted and top-down SEM images of circle and square nanotubes with different diameter sizes (b, c), custom-arranged hollow nanobricks (d, e), flower-shaped nanostructures array composed of elliptical nanotubes (f, g), complicated hybrid-structures including pillars and nanotubes with various shapes (h, i), and tree-shaped and irregular nanostructures (j, k). SEM images of well-defined large-scale arrays of nanotubes on Si substrate (h) and on flexible aluminum film substrate (l), with a local enlarged image inserted in the center. Scale bars, 1 µm.

controllability. Si patterned template is firstly used by ALD assisted nanofabrication, but it requires a perfect combination of lithography and dry-etching as well as removing process of Si so that its diversity and controllability in template shapes is very limited, and the whole process is also complicated [22–24]. The porous AAO template-assisted technology is another interesting approach to fabricate large arrays of nanostructures, where an AAO template is utilized as a rigid scaffold. AAO technology has desirable characteristics such as easy controllability of an interpore distance, a pore diameter and a pore depth by changing the anodization conditions [12,25–27]. Current existing AAO template assisted technology is usually applied to produce very simple nanostructures such as single nanorod or nanotube structures and also realize the complex patterns and structures but need very complicated process, greatly limiting their applications and functionalities [28,29]. Generally, imprinting process are crucial steps to fabricate the AAO template, but imprinting template need multistep process including lithography and etching as well as transfer techniques, which make the process more complicated. Additionally, AAO templates is hard to be formed directly on the Si substrates and also inevitably encounter some problems of complicated post processes, and the removal of the AAO template using chemical solvent is a big trouble to be compatible with the fabrication of conventional Si-based integrated circuits.

Based on rigid templates, above common problems faced by ALD assisted nanofabrication are how to select more flexible templet materials and greatly simplify the nanofabrication processing steps. Instead of rigid templates, some soft templates are introduced into ALD assisted nanofabrication to form free-standing nanostructures, such as block polymer [30,31], photo resist for direct laser writing or proximity field nanopatterning [32–36], even PS nanosphere [37,38], which show a more flexible and simpler approach than rigid templates to construct the nanostructures. However, these soft templates still have some obvious limitations in compatible controlling the nanostructure diversity, small feature size, higher fabricating accuracy, irregular shapes and aperiodic array of the resulting nanostructures.

To break through the discussed limitations of traditional techniques utilizing rigid templates and previous soft templates, we present an atomic layer assembling fabrication (ALAF) method relied on electron beam resist (EBR) soft-template to fabricate complex multiple nanostructures on various substrates by atomic layer deposition assembling. Here, the EBR is used to make soft-templates on almost any substrates, even flexible substrate, also meaning that various nano-patterned templates can be fabricated directly by electron beam lithography (EBL). Additionally, the heat resistance of EBR basically conforms to the deposition temperature of ALD. Thus, the advantages of ALD deposition are combined with high precision fabrication of EBL, which can greatly improve the capability of ALD assisted nanofabrication, resulting in high resolution down to nanometers and ultra-high aspect ratio of hundreds. More advantages of atomic layer assembling versatile nanostructures in EBR soft-templates also include high variability and multiformity of the patterns, extreme nanofabrication, convenient and efficient fabrication process, material diversity and easily removing soft-templates. Based on mature planar fabrication processing, soft-template structures in nanoscale can be freely patterned by EBL, in which precisely controlled ALD can assemble desirable nanostructures along three dimensional directions, and then a dry etching process removes soft scaffold and leaves freestanding multiple 3D nanostructures with tunable size, shape and spatial arrangement. With our ALAF approach, we also design and fabricate an optically active all-dielectric metasurface and ultra-sensitive hydrogen gas sensor, demonstrating their high performances. Therefore, our proposed ALAF method raise greatly the level of controllable nanofabrication for novel multiple nanostructures and multi-material hybrid nanostructure and give many diverse possible combinations of dimensions, materials and morphologies using the EBL and ALD towards a broad application in modern nanodevices.

Results and discussion

Fig. 1a shows a schematic of the ALAF processes, including four steps, from EBL and ALD to dry etching and removing resist. The patterned soft-template is firstly formed by EBL to provide space for next atomic layer assembling, and dry etching is used to eliminate the surface layer of filled soft-template to prepare for removing resist. The nanostructure assembled by ALD is completely dependent on the EBL patterns. More details in fabrication processes are described in the Methods Section. Based on above ALAF process, large-scale arrays of various complex 3D nanostructures with different sizes and shapes are designed and obtained, and TiO_2 is chosen as a typical material to configure multiple 3D nanostructures here. Representative as-assembled 3D nanostructures are displayed in Fig. 1b-k, reflecting fully diversity of nanostructure control. Firstly, Fig. 1b and 1c show that a hybrid array of circle and square nanotubes with various diameter sizes from 100 nm to 160 nm are fabricated simultaneously, and as-obtained wall thickness could be as small as 25 nm with the height of 800 nm, having a very high aspect ratio of 32 for nanotube wall. What's more, the arrangements of the designed 3D nanostructures are flexible and customized. As shown in Fig. 1d and 1e, hollow nanobrick arrays with gradually turning $\pi/4$ increase of angle are fabricated, and its hollow construction can also be filled to solid one with tunable angle arrangement, which would play an important role in applications of artificial nanophotonics devices. Fig. 1f and 1g show flower-shaped nanostructures array composed of elliptical nanotubes, displaying powerful diversity of forming images. More complicated combinational structures of circle pillars and different shaped nanotubes are shown Fig. 1h and 1i, in which the span of this structural scale is relatively large from 60 nm to 1 μm, reflecting a cross-scale fabricating capability. In addition of above periodic arrays of 3D nanostructures, ALAF can fabricate more complex and irregular images. As shown in Fig. 1j and 1K, tree-shaped nanostructure is designed and prepared, and its perfect local structure features indicate good fabricating flexibility and precision though the image is complex and irregular, having a potential to imitate complex liquid flowing micro/nano-channel in the organism. Further, the large-scale controlled fabrication of complicated and customized nanostructures is another advantage of the ALAF method, no matter how complicated the exposed patterns are. Fig. 1h show an array element of well-defined TiO_2 nanotubes with the area size of $50\times50\,\mu m$, having very good repeatability and the stability. Particularly, the 3D nanostructures can also be fabricated on flexible substrates. As shown in Fig. 1l, TiO_2 nanotubes are formed on flexible metal aluminum film substrate without any structure distortion and, of course, on other soft-substrate, indicating a promising potential in flexible wearable devices.

Thus, it can be seen that the flexibility and controllability of EBL techniques in preparing nanostructure enable ALD powerful assembling ability and freedom, and hence versatile complicated structures with multiple shapes and sizes, especially including diversiform regular and irregular or solid and hollow, can be designed and fabricated smoothly by ALAF method on the same substrate simultaneously. This powerful and flexible controllability in nanofabrication technique paves the way to multifunctional device applications. Furthermore, the limitation of this method maybe the long-time consumption originating from EBL and ALD in large-area fabrication, which is attributed to the self-feature of EBL direct-writing technology in producing nanostructures and low deposition rate of ALD. However, the EBL time consumption might be reduced by combining with other techniques, like nanoimprinting, by which EBL is only utilized once to fabricate the stamp. What's more, the ALAF method is not also confined to EBL, the photolithography could

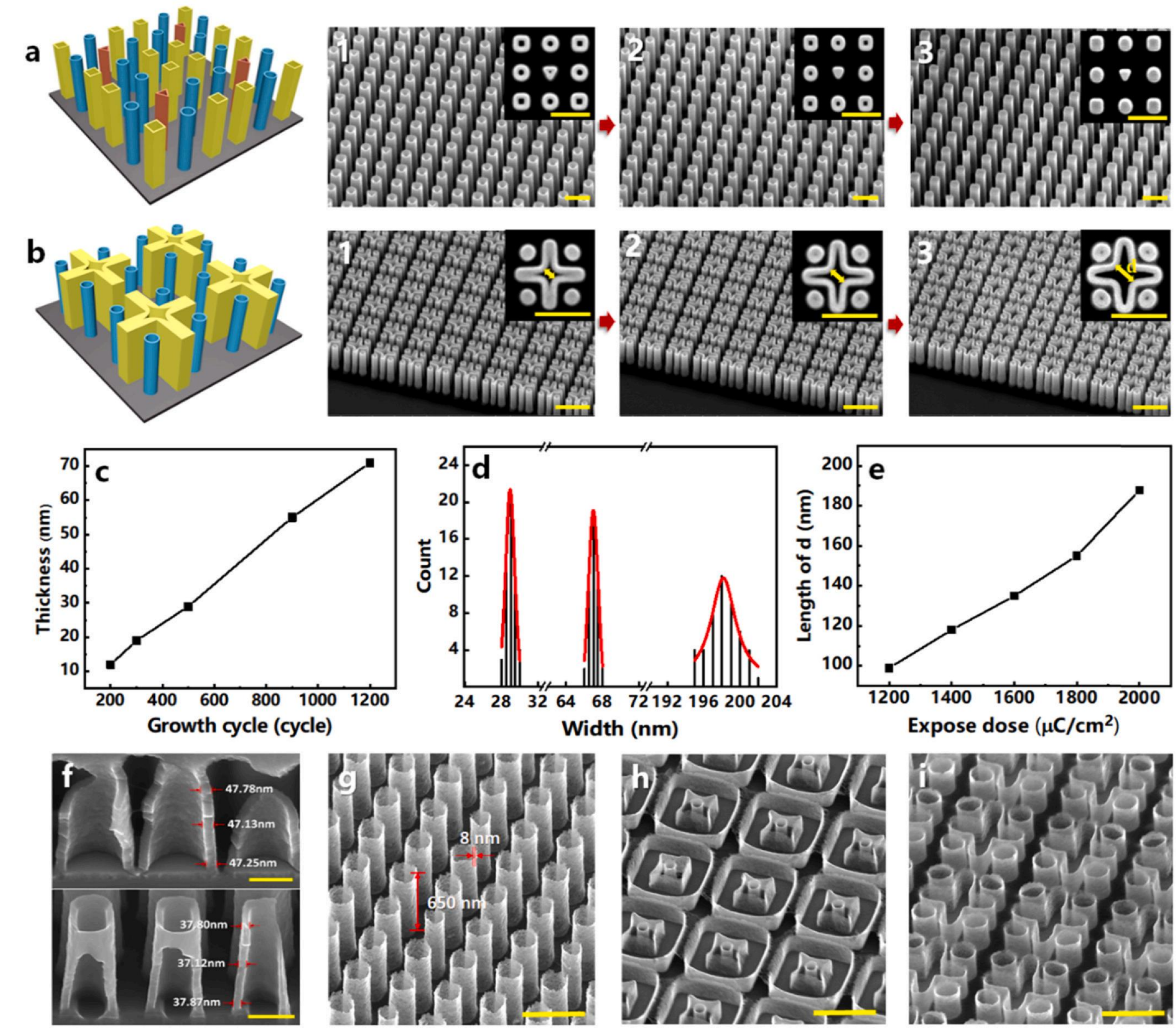

Fig. 2. Effect of ALD cycles and EBL exposing doses on the feature of as-formed nanostructures and extreme processing of ALAF method. (a) Illustrations of hybrid columnar nanostructures with three kinds of cross-section shapes including circle, square and triangle, marked by blue, red and yellow. (a1, a2, a3) Tilted SEM images of columnar structures assembled by ALD using increased cycles of 500, 1200 and 1900, respectively. The insets are the corresponding enlarged top-down SEM images，indicting a morphologic change from hollow to solid. (b) Illustration image of composite structures with shapes of cross and circle. (b1, b2, b3) Tilted SEM images of structures with different exposing doses of 1200, 1600 and 2000 μC/cm^2, respectively. The enlarged top-down SEM images are inserted, in which *d* is the width of the center area in the cross. (c) Dependence of the wall thickness of columnar nanostructures on ALD growth cycles. (d) Histogram depicting the distribution of wall thicknesses of columnar structure at 500, 1200 and 1900 ALD cycles, which are obtained by measuring 48 square nanostructures in a1, a2 and a3, respectively. (e) The relationship between exposing doses and the width (*d*) in the center of the cross. Scale bars, 500 nm. (f) The uniformity of the oxide films used in ALAF method is shown in cross-sectional SEM image of the nanotube. Scale bars, 200 nm. (g- i) The extreme processing of ALAF method. Vertically ultrathin nanostructures arrays with various patterns are shown, having an 8 nm wall thickness and the highest height of 650 nm. Scale bars, 500 nm.

also be utilized in the ALAF for low-cost and high-throughput applications but having a low structural resolution.

For ALAF process, ALD cycles and EBL exposing doses are two key factors in structural regulation, determining the features and details of as-fabricated nanostructure. Fig. 2a shows the effect of ALD cycles on as-formed columnar nanostructure, containing ternary cross-section shapes of circle, square and triangle, along with a transform from hollow to solid. The diameter of the circle, width of square, and side length of triangle are designed as 180 nm, 180 nm and 150 nm, respectively, which are combined to form a hybrid patterned array by EBL as soft-templet. The 500 cycles of TiO_2 film are firstly deposited by ALD process at 105 °C to assemble and fill in the soft-templet. After removing the top-cover of TiO_2 and the residual resist, different shaped TiO_2 nanotubes with a high aspect ratio are obtained, as shown in Fig. 2a-1. With increasing ALD cycle number, the features and details of as-formed nanotubes are regulated. When growth cycle number is total 1200 cycles, the small triangle nanotubes are filled up and transformed to nanopillars, and thus large-scale arrayed binary nanostructures with nanotubes and nanopillars are produced simultaneously, as shown in Fig. 2a-2. Finally, all the nanotubes are filled up and transformed to nanopillars with differ cross-section shapes after 1900 cycles (Fig. 2a-3). It revealed that under fixed structure size of soft template, the ALD growth cycle can affect greatly the morphologies of as-form nanostructure from

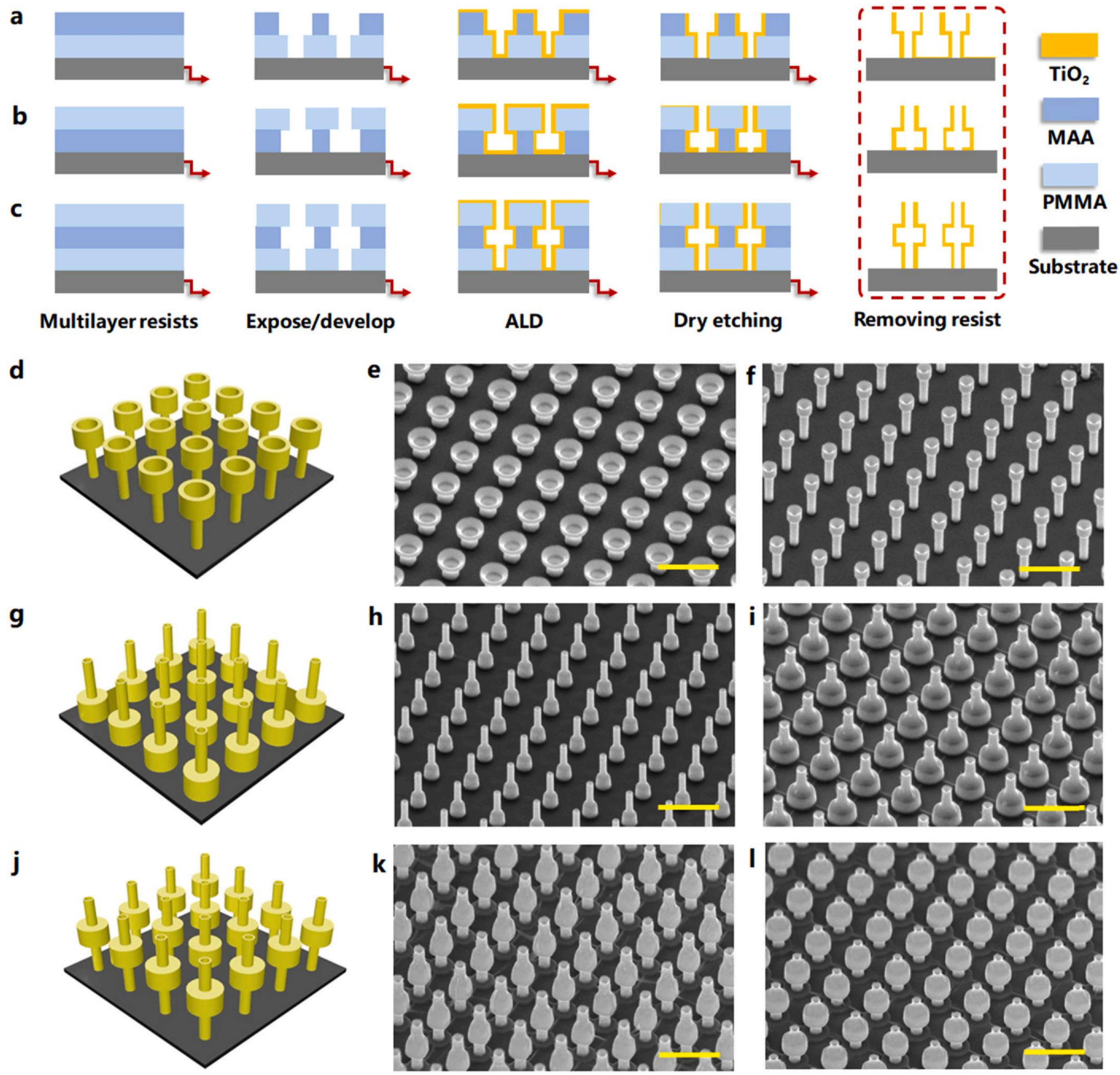

Fig. 3. Diameter-modulated cylindrical hollow nanostructures formed by ALAF method. (a, b, c) Fabrication process of structures with three variable diameter shapes, including from large-top to small-bottom, from small-top to large-bottom and large-middle with small both ends. Illustration and tilted SEM images of structures with large-top and small-bottom shapes (d, e, f), with small-top and large-bottom shapes (g, h, i), and with large-middle and small ends shapes (j, k, l) under different sizes. Scale bars, 1 µm.

hollow to solid, such as changing nanotubes to nanopillars in this case.

The ALD growth thickness also shows a linear dependence on the growth cycle, as shown in Fig. 2c. What's more, by measuring the widths of 48 nanostructures with a square cross section in Fig. 2a1-a3, the distribution of their structure widths corresponding to 500, 1200 and 1900 growth cycles are indicated in Fig. 2d, respectively. We can find that the square nanotube widths of 500 and 1200 growth cycles are 29 ± 1 nm and 67 ± 1 nm, respectively, showing very good accuracy and consistency in structural control due to a self-limiting surface reaction. However, when all the nanotubes are filled up and transformed to nanopillars after 1900 growth cycles, the widths of the square nanopillars are 198 ± 3 nm, which is larger than the designed 180 nm. This was because that the width of the nanopillars is dependent on the sizes of resist holes obtained by EBL process, instead of the ALD cycles anymore. And the exposing and developing process should be responsible for the size expansion and the lower thickness precision.

Furthermore, the exposing dose of the EBL process also shows great control ability over the structural morphologies in the ALAF method. Composite nanostructures consisting of the cross and circle are designed and illustrated in Fig. 2b. The SEM images of structures with different exposing doses of 1200 µC/cm^2, 1600 µC/cm^2 and 2000 µC/cm^2 are revealed in Fig. 2b1-b3, respectively. It can be seen that when the exposing dose increases from 1200 µC/cm^2 to 2000 µC/cm^2, the distance (d) in the center of the crossed nanostructures is increased from 99 nm to 188 nm to enlarge the shape size of the cross, and the diameters of the circled nanostructures next to the cross is increased from 141 nm to 172 nm at the same ALD growth circles. Fig. 2e displays the near-linear relationship

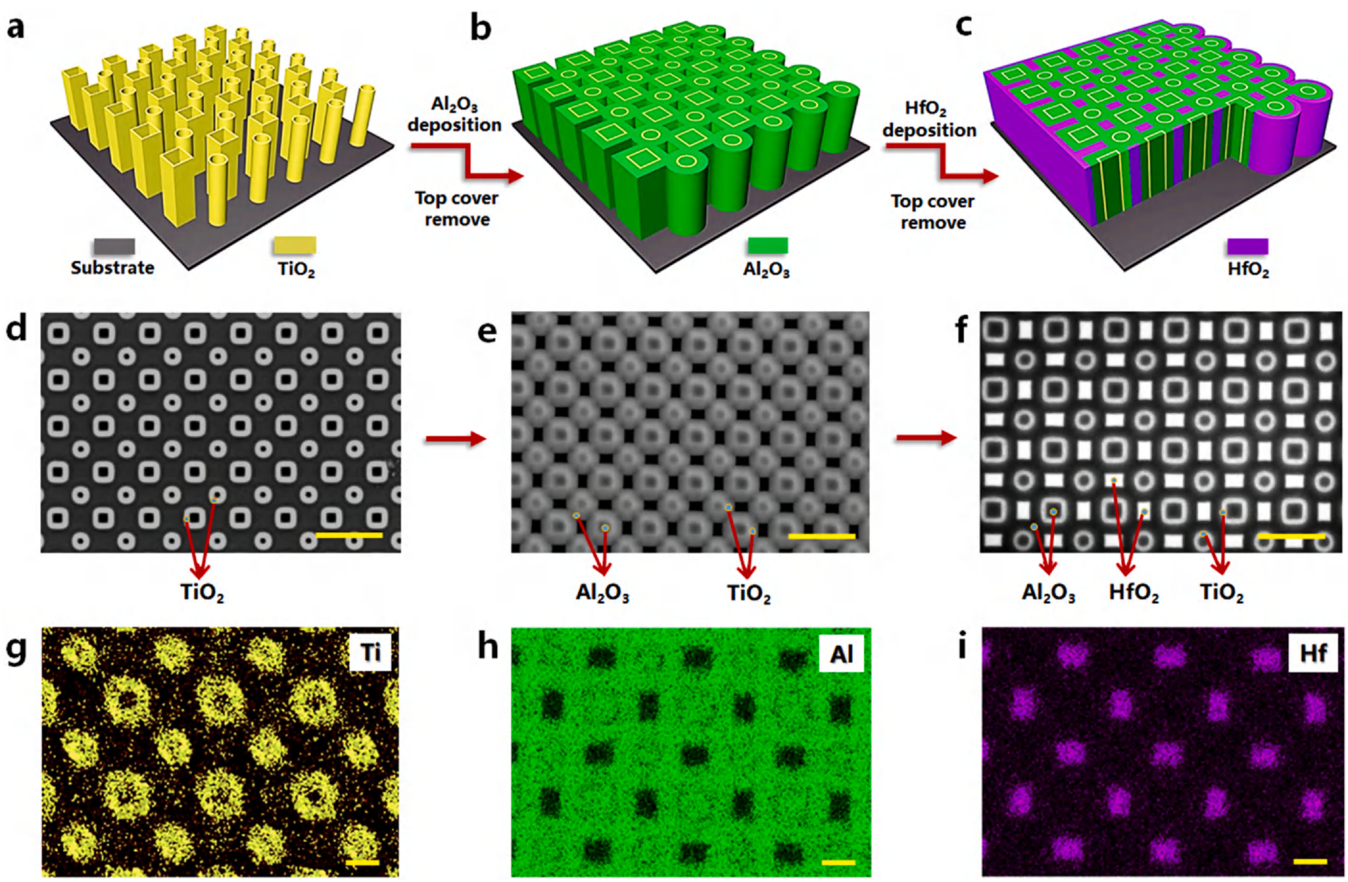

Fig. 4. Illustration and top-down SEM images of TiO_2 nanotubes with two shapes of circle and square (a, d), TiO_2 nanotubes surrounded by Al_2O_3 deposited by ALD (b, e), and hybrid structures formed by TiO_2, Al_2O_3 and HfO_2 using ALAF method (c, f). (g, h, i) EDX maps of this hybrid structure, showing Ti (yellow), Al (green) and Hf (purple) mapping images, respectively. Scale bars, 1 μm.

between *d* and exposing dose, ignoring the shape distortion induced by the influence of the cross during the EBL process. Particularly, when the exposing dose is 1200 μC/cm^2, the circle resist holes are fully filled up to form the circle nanopillars (Fig. 2b-1), however, the nanopillars is transformed to nanotubes as the exposing dose reaches to 2000 μC/cm^2 (Fig. 2b-3). From the above results, it can be seen that the transformation between nanotubes and nanopillars can be controlled by not only adjusting the designed size and growth cycle, but also by the exposing dose, which enables the ALAF method to be a simple way to fabricate complicated 3D nanostructures.

Fig. 2f shows the cross-section SEM image of the nanotubes with the same height of 800 nm and different wall thicknesses of 37 nm and 47 nm before and after the top cover removal, respectively. Along the tube wall with marked thickness from top to bottom in cross-sectional SEM image, it can be seen that the uniformity of the oxide films is quite excellent with a thickness difference of less than 1 nm, which can ensure the corresponding properties consistent with the simulating results. In particular, by means of the high resolution of EBL and ultra-high precision thickness control of ALD, an extreme structural nanotube array is assembled successfully, having an 8 nm wall thickness and the highest height of 650 nm with an ultra-high aspect ratio of more than 80:1, as shown in Fig. 2g. This ultrathin wall is almost transparent and has no any distortion or collapse. Other kinds of vertically ultrathin nanostructures with various patterns are designed and fabricated (Fig. 2h and 2i), demonstrating a strong extreme processing ability of ALAF method, which is beyond the limits of EBL nanofabrication.

Generally, to fabricate precisely diameter-modulated hollow nanostructures are a very big challenge for traditional fabricating method [39,40], however, ALAF method has prominent advantage in realizing these complicated 3D nanostructures. The key technology of this method is to use different kinds of multilayer photoresists in EBL process, such as the polymethymethacrylate (PMMA) and copolymer P(MMA 8.5 MAA) photoresist in the work. Relying on different exposing sensitivities, the order, number of layers and thickness of two kinds of resists possess the dominant influence and determine the final shape of the variable diameter nanostructures. The whole fabrication processes with typical three kinds of diameter-modulated hollow nanostructures are illustrated in Fig. 3a-c. Firstly, PMMA and P(MMA 8.5 MAA) resists are orderly spun on the substrate in certain order. Then big patterns at the top are exposed on the resists using a low dose, followed by another exposure of small patterns at the bottom using a large dose on the same position. Due to the high exposing sensitivity of the P(MMA 8.5 MAA) resist and low exposing sensitivity of the PMMA resist, big patterns with low dose could only induce the corresponding exposed area in the P (MMA 8.5 MAA) resist to degrade. However, the small patterns with large dose would induce all the exposed areas, both in the PMMA and P(MMA 8.5 MAA) resist, to degrade. After that, ALAF method is utilized to assemble the complicated structures along 3D freedoms in as-patterned resist structures as a soft-template. By changing the order and the number of layers and adjusting the thickness of the photoresists, three kinds of diameter-modulated hollow nanostructures are fabricated smoothly.

More fabrication details in preparation process are described in the Method Section. The illustrations and tilted SEM images of as-formed three diameter-modulated structures with different sizes are shown in Fig. 3d-l, including from large-top to small-bottom, from small-top to large-bottom and large-middle with small both ends, respectively, having very good uniformity , flexibility and variability in controlling structure. More designs in feature size and shape control of these nanostructures can be realized by above way to prove the powerful capability of ALAF method in configuring 3D nanostructure. Further, these diameter-modulated tubular nanostructures can be potentially utilized in applications of efficient light harvesting devices [41], nanobionics, nanofluid-channel, and nanobiology devices.

Multimaterial hybridization is another advantage of the ALAF method to construct desired nanostructure and meet the processing needs of complex devices. Here, three kinds of materials, such as TiO_2, Al_2O_3 and HfO_2, are selected to design and fabricate the multimaterial hybridized nanostructure. Firstly, separated TiO_2 nanotubes are fabricated by ALAF method, as illustrated and shown in Fig. 4a and 4d, respectively. Afterwards, Al_2O_3 layer with certain thickness is deposited by ALD on the sample, all the surfaces of the TiO_2 nanotubes are covered with Al_2O_3. Meanwhile, the spaces between TiO_2 nanotubes are still not fully filled, as shown in Fig. 4b and 4e. Then dry etching process is conducted using BCl_3 and Cl_2 to remove the Al_2O_3 both on the nanotube top surface and bottom of the unfilled space, followed by a third ALD process to deposit HfO_2 to fill the unfilled space to form columnar structure with quasi-rectangular cross section. Finally, another dry etching process is conducted to remove the HfO_2 on the top surface. Thus, the close packed 3D structures with three kinds of materials are obtained, as shown in Fig. 4c and 4f. It can be seen that the HfO_2 nanopillars are separated from the TiO_2 nanotube by Al_2O_3 filler. The discrete distribution of the Ti, Al and Hf elements is further supported by energy-dispersive X-ray spectroscopy (EDX) maps in Fig. 4g-i, respectively. Therefore, this novel 3D nanostructure with discrete distribution of different materials by ALAF method shows outstanding features in multimaterial hybridization and enable great potential applications in fabricating discrete devices, like gate-all-around field effect transistor [12] and integrated circuit. In 3D nanostructures for electronic devices, reliable contacts at the electrode/active materials will be important, and a feasible strategy is that both electrode and active materials are prepared by ALAF methods to ensure reliable contact. On the other hand, the materials-related limitation in the ALAF method is a vital issue for next device application. Many materials can be deposited using ALD in the ALAF method, such as various oxide materials TiO_2, Al_2O_3, HfO_2, ZnO, Cu_2O and ZrO_2, etc. From current ALAF method based on soft-templates, ALD materials at the deposition temperature of lower than 120 ℃ can be utilized in the ALAF method, however, the materials deposited by O_3 precursor or plasma-enhanced ALD method are not suitable to ALAF because these can damage the EBR soft templates.

From the above, the ALAF method shows extremely powerful processing and control capability for multiple 3D nanostructures, and also paves a feasible way for their corresponding multifunctional characteristics and device applications. As an example, the metasurface is highly dependent on the design and regulation of surface structure. And especially for dielectric metasurface working in the visible and near-infrared region, their shape and size, high aspect-ratio, plane rotation-angle and arrangement of nanostructure cell in the metasurface affect greatly the light field regulation characteristics [42–44] and thus have higher requirements for nanofabrication. Facing to the challenges in the nanofabrication, ALAF method can fully meet this requirement.

Here, we proposal firstly an optically all-dielectric metasurface to manipulate the transmitted vector beam over a broadband wavelength range in the visible region, based on high aspect-ratio TiO_2 nanofins fabricated by ALAF method, as illustrated in Fig. 5a1. The designed metasurface includes two supercells (I and II), which can easily modulate the polarization states of vector beams by different angle rotations of the nanofins in the different unit-cells, as displayed in Fig. 5a2. The unit cells are arranged with periods P = 400 nm, and two supercells in the transmission metasurface have eight unit-cells with opposite direction of rotation. It is clear that the supercells with different directions of rotation could modulate the different polarizations of the beams. According to the Pancharatnam-Berry (PB) phase, the phase of the scattering of light with opposite spins equals to the twice the orientation angle of the nanofin [45–47]. In this way, the diffraction of the light will separate with opposite direction due to the different orientations of nanofins. Fig. 5a2 shows that the metasurface include periodic I and II supercells arranged alternately along y direction. In supercell I and II, there was π/8 rotated angle between the two neighbor nanofins along x-axis. When the linearly polarized light with polarization direction paralleled to the x-y plane is normally incident onto the metasurface, the different rotation of the supercell could make the corresponding circular polarized component anomalous refracted. Further, the diffraction of ± 1 orders of incident light will be separated in the opposite direction after it passed the metasurface. It is noted that the goal can be achieved through splitting the circular components of the incident beam and introducing an optical phase delay δ between the opposite polarizations. At the same time, the polarization angle (PA) φ is tunable by changing the phase delay δ. Linear polarized light with a PA φ can be written in terms of its circular components as $E = E_0(\hat{x}\cos\varphi + \hat{y}\sin\varphi) = \frac{E_0}{\sqrt{2}}(\hat{r}e^{-i\varphi} + \hat{l}e^{i\varphi})$, where $\hat{r} = (\hat{x} + i\hat{y})/\sqrt{2}$ and $\hat{l} = (\hat{x} - i\hat{y})/\sqrt{2}$ are represent RCP and LCP, respectively. The equation indicates that a phase delay of 2φ introduced to the RCP with respect to LCP will rotate the PA by φ. In addition, due to the opposite nanofins orientation of the two supercells, the LCP and RCP components are transmitted to the same side. Then, LCP and RCP from different supercells add up together to retrieve linearly polarized light. The output light obtains a 180°·δ/s polarization rotation because of the phase shift between the two supercells, where the s is the length of the supercell. Fig. 5b have shown the SEM images of four different samples S1, S2, S3 and S4, in which the phase shift δ between the neighbor supercells are 0, π/4, π/2, 3π/4, respectively. Most interestingly, transmitted rotation angle only depends on the lateral spatial shift between the I and II supercell due to no dispersion in the measuring wavelength, which is shown by geometric phase.

Fig. 5c shows the theoretical distributions of vector beams after passing through polarizer S0, sample S1, S2, S3 and S4, followed by a longitudinal linear polarizer, respectively. As shown in Fig. 5d1, we convert a linear light into a donut beam by a polarizer in order to verify the manipulation of the polarization state of the vector beams with the metasurface. And the donut beam would distribute like Fig. 5e1 after passing through a longitudinal linear polarizer, whose direction is indicated by the double-headed arrow. Similarly, when the light passes through sample S1, S2, S3 and S4, the directions of polarization of vector light are along the arrows, which are shown in Fig. 5d1–4, respectively. Fig. 5e1–4 show the fan-shaped pattern with different directions corresponding to four different samples after passing through longitudinal linear polarizer, following the polarization of Fig. 5d1–4 due to the modulation of the vector beams, which is according well with the theoretical distributions. Specially, when the light passes through sample S1 followed by longitudinal linear polarizer, the distribution of vector beams is the same as that of polarizer S0, which is corresponding to the zero-geometric phase shift Δ. Thus, this TiO_2 nanofins metasurface can realize the arbitrary polarization control theoretically, showing high-performance and great potential for applications involving vector beams, such as microscopy imaging, optical trapping and quantum communications. Compared with other nanostructures-based metasurface, the current structures fabricated by ALAF shows some advantages, such as high resolution, high aspect ratio, high variability and multiformity, and fabricating challenging complex 3D nanostructures, which greatly meets the needs of the achieving complicated metasurface devices with multifunction and high-efficiency.

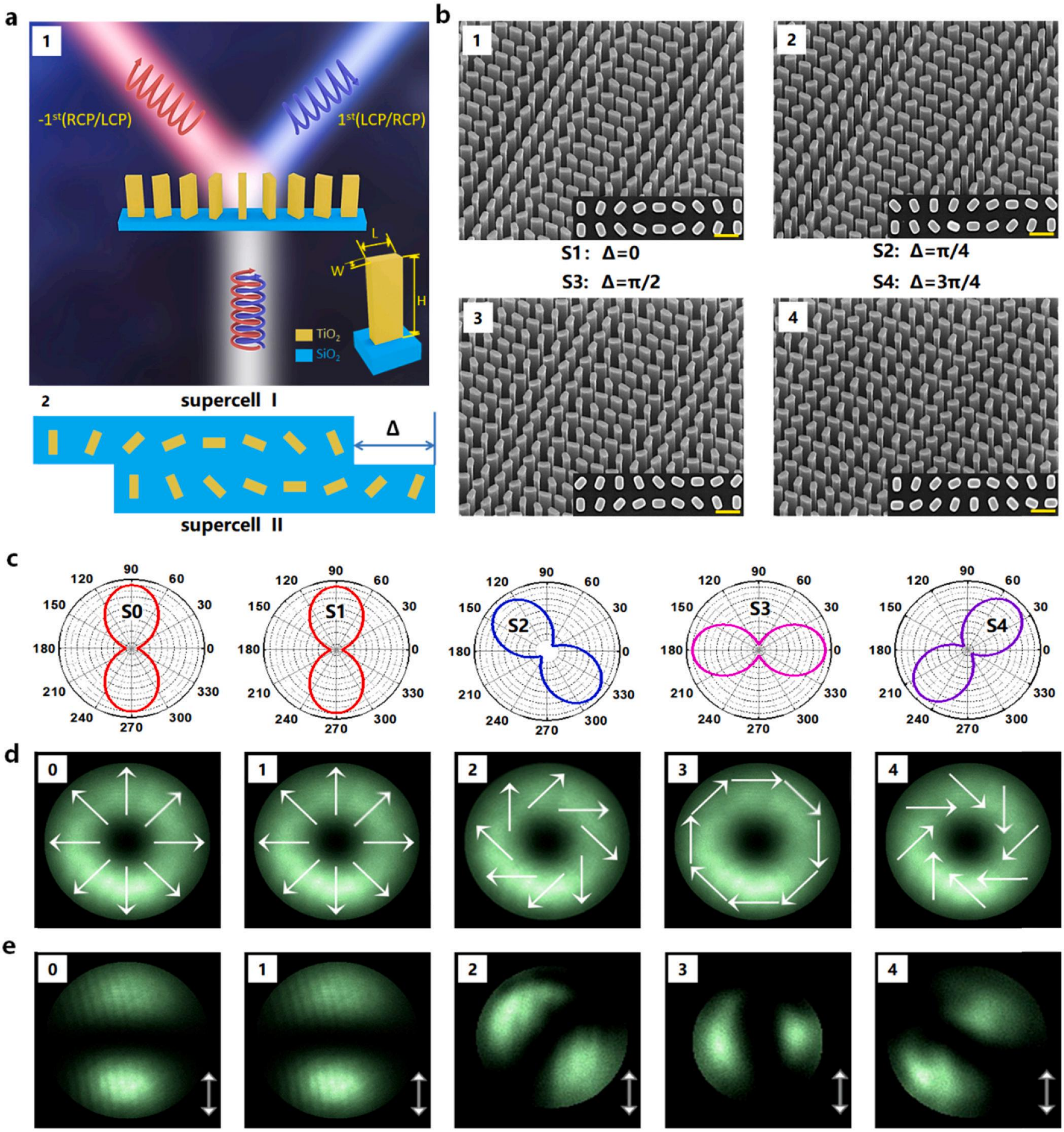

Fig. 5. (a1) An illustration of as-designed TiO_2 metasurface. The right/left-handed and left/right-handed circularly polarized components will be diffracted into the (±1) first diffraction orders after a linearly polarized light transmitted by the metasurface I/II. The inset shows the unit cell of the structure, which is consisted by quartz substrate and the TiO_2 nanofin. (a2) Each unit I or II contains eight nanofins with π/4 increase of the angle, though they are in opposite direction. The transmitted linear polarization direction in the first diffraction orders can be realized by introducing a geometric phase shift Δ between the supercells I and II. (b1 - b4) SEM images of different nanofins with different phase shifts. The phase shifts Δ of the sample S1, S2, S3 and S4 are corresponding to 0, π/4, π/2 and 3π/4, respectively. The scale bars are all 500 nm. (c) Theoretical distributions of vector beams after passing through polarizer S0, sample S1, S2, S3 and S4, followed by a longitudinal linear polarizer, respectively. (d0 – d4) The intensity distribution of the incident light which has passed through the polarizer S0, sample S1, S2, S3 and S4, respectively, with the white arrows representing the polarization of the beam. (e0-e4) When a longitudinal polarizer is used, the distribution of vector beams with longitudinal polarization in the (d0-d4) is mapped.

It is well known, multi-material compositeness is very important for constructing 3D nanostructure devices and enabling it robust function, which is just a strength of ALAF method preparing multiple 3D nanostructures. Based on the mechanism of 2D electron gas (2DEG) at the interface of a heterostructure Al_2O_3/TiO_2 thin film, this can be combined with Palladium (Pd) as high-performance hydrogen (H_2) gas sensor [48,49]. Here, Al_2O_3/TiO_2 hexagram hollow nanostructures arrays with a high aspect ratio are designed and fabricated by ALAF method, and then Pd nanoparticles (~2 nm in thickness) are coated on the inner and outer walls of the nanotube by electron beam evaporation, as illustrated Fig. 6a. From the cross section of this 3D heterogeneous nanostructures, TiO_2 is a main material of

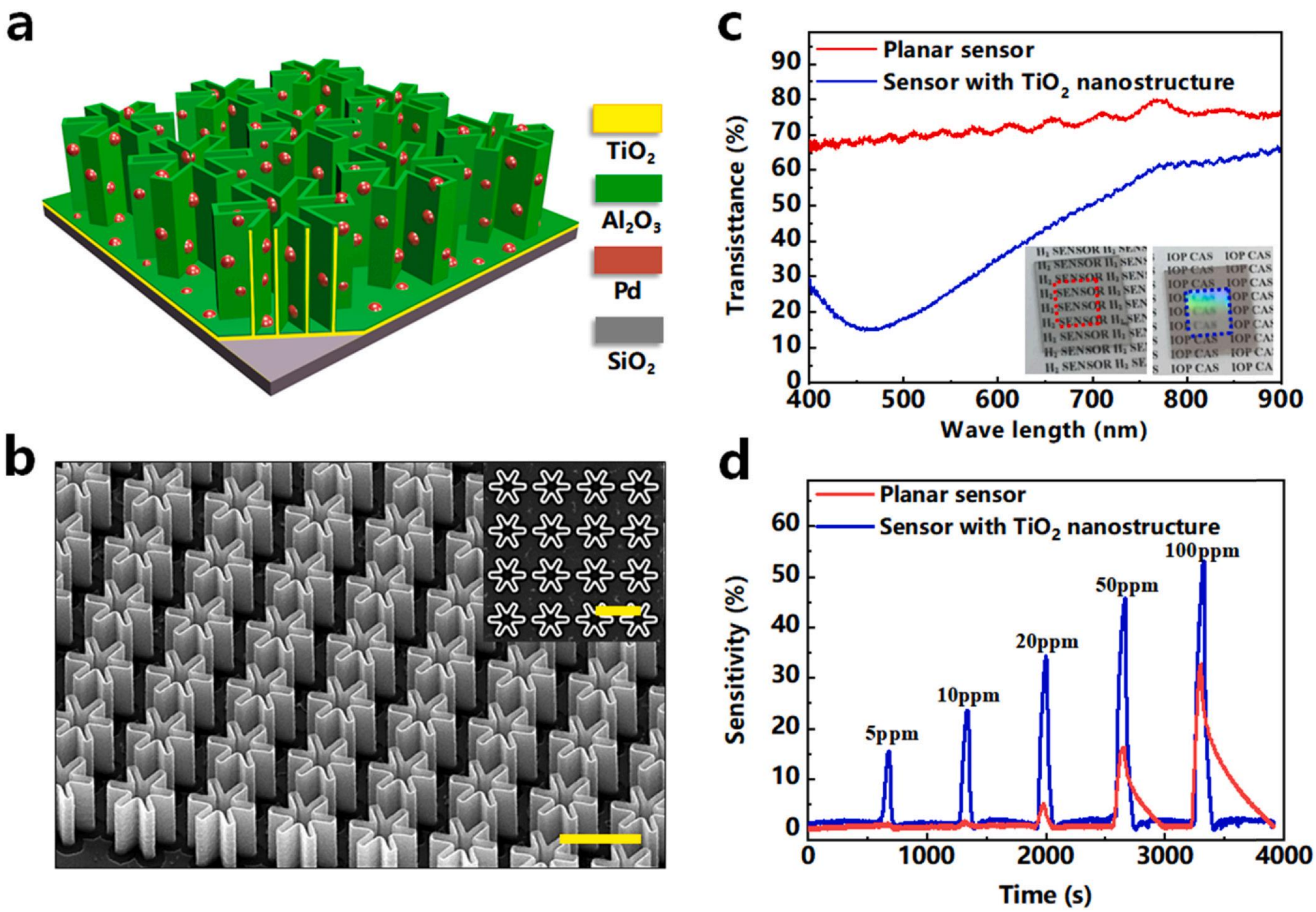

Fig. 6. (a) Illustration of as-fabricated gas sensor with $Pd/Al_2O_3/TiO_2$ hexagram hollow nanostructure arrays, a longitudinal section showing a heterostructural feature in the nanostructure. (b) Titled SEM images of as-fabricated gas sensor with $Pd/Al_2O_3/TiO_2$ nanostructure corresponding to the illustration, and the inset is the top-down SEM image of this nanostructure. (c) The transparencies of obtained gas sensors with and without high aspect-ratio $Pd/Al_2O_3/TiO_2$ nanostructures are as high as 62% and 76% at 760 nm wavelength, respectively. The insets are the real photographs of as-fabricated planar (left) and nanostructure (right) gas sensors. (d) Sensitivity of $Pd/Al_2O_3/TiO_2$ gas sensor as a function of various H_2 concentrations. Scale bars, 1 μm.

nanostructures, and the thickness of Al_2O_3 layer will be controlled very thin (~3 nm) to cover both the inside and outside surfaces of the TiO_2 wall to form 2DEG on both sides. The detail fabrication process is described in the Method Sections. Fig. 6b shows as-formed $Pd/Al_2O_3/TiO_2$ nanostructure arrays with a hexagram hollow cross-section, having fine structure control and perfect uniformity. Meanwhile, a planar $Pd/Al_2O_3/TiO_2$ gas sensor is also fabricated to compare with nanostructure gas sensor.

The transparency of as-formed gas sensors with and without nanostructure arrays are respectively as high as 62% and 76% at 760 nm wavelength, and two inserted photographs are real gas sensor samples, as shown in Fig. 6c. This transparent gas sensor has important application potential as they are combined into transparent devices, such as smart windows [50]. The sensitivities of two types of sensors are measured at different H_2 concentration under a temperature of 80 °C, and the detailed measurement process is described in the Method Sections. The sensitivity is defined as the relative change in the current flowing through the 2DEG at the interface of the Al_2O_3/TiO_2 heterostructure, before and after H_2 gas adsorption. Thus, the sensitivity (%) = $\Delta I/I_0 \times 100$, $\Delta I = I - I_0$, where I indicates the current during H_2 adsorption and I_0 indicates the current during operation without H_2 adsorption. As shown in Fig. 6d, we can see that the sensitivity of the sensor with nanostructure arrays can reaches to 15.5% at ultralow H_2 concentration of 5 ppm with a fast response time of 60 s and recovery time of 36 s, demonstrating ultrahigh detection capability for H_2. The sensitivity and response time of our sensor with nanostructure arrays at relative low temperature are comparable to those from the best reports that operated at 200–400 °C [48,51], and especially, our results exhibit the shorted recovery time compared to the latest best planar $Pd/Al_2O_3/TiO_2$ sensor [48] of 245 s. What's more, it should be emphasized that 3D nanostructure sensor shows an enhanced sensitivity, which is nearly 31 and 3 times higher than that of planar sensor at 5 ppm and 50 ppm, respectively. Therefore, 3D H_2 gas sensor with nanostructure array shows a great improvement over the planar sensor, which makes it more efficient for H_2 detection.

The sensitivity as a function of time for as-formed gas sensors with nanostructure arrays is also measured under repetitive injection of H_2 (10 ppm), exhibiting a reliable detection (a sensitivity of 24% is sustained after repetitive injections of H_2) with repetitive cycles. It is well-known that Pd is a good sensing material with high selectivity and anti-interference for H_2 detection due to the formation of PdH_x during H_2 injection [52–54]. The decreases of work function induced by PdH_x formation increase the conductance at the interface of the Al_2O_3 /TiO_2, which decreases the 2DEG resistance because the electrons from the Pd nanoparticles move to the surface of the TiO_2 layer through thin Al_2O_3 layer [47]. Consequently, this effective tuning of the 2DEG electron density on the Al_2O_3/TiO_2 heterostructure optimize the sensitivity for H_2 detection. In addition, the high aspect-ratio tubular nanostructures enlarge greatly the surface area for the reaction between Pd and H_2 through their inner and outer walls, which is also mainly responsible for the improved sensitivity. Thus, by coating Pd nanoparticles on the Al_2O_3/TiO_2 nanostructure based on ALAF method, we demonstrate a high-performance and transparent H_2 gas sensor with very quick response and recovery at low temperature, which is comparable to those from the best reports and a promising candidate for H_2 sensor, exhibiting more potential abilities in special multi-layer composited 3D gas sensors with high performances.

Conclusion

In summary, by exploiting versatile soft-template combined with atomic layer assembly, we have presented a simple and scalable ALAF method to realize complex multiple 3D nanostructures, which can be solid or hollow, demonstrating its good control of material diversity, structure variability and scalable fabrication. Especially, novel diameter-changed nanostructures and proof-of-principle 3D nanostructure with discrete distribution of different materials are simply and conveniently manufactured by ALAF method, showing powerful nanofabrication ability and outstanding features in multiple structures and multimaterial hybridization, which not only enable great potential applications in more modern nanodevices, but also can in turn be used to guide the design of advanced nanostructures. To underline the potential of this simple assembly fabrication for these 3D configurations, we demonstrate a high-performance all-dielectric metasurface to manipulate perfectly transmitted vector beam over a wideband wavelength range in the visible region. In addition, an ultra-sensitive hydrogen gas sensor with multilayer composited nanostructures is also formed by ALAF, showing a great improvement of sensitivity and efficiency far more than that of planar sensor. This approach enables the conventional lithography or assembly techniques to possess new powerful functionalities and more abilities in nanofabrication, which put up a powerful platform to reconcile a new flexible 3D nanofabrication with versatile and multiple nanostructures towards broad potential applications in nanophotonics, nanosensing, nanoelectronics, and nanobionics devices.

Experimental section

Fabrication of nanostructures

In the ALAF method, silicon, quartz or even the flexible PI substrates are used to fabricate the 3D nanostructures, which are cleaned in acetone, isopropanol (IPA) and deionized water in sequence. Successively, the polymethyl methacrylate (PMMA) resist 950-A7 are spun at 3000 rpm and baked at 180 °C for 2 min. Various patterns combined by different sizes and shapes are exposed using electron beam lithography system (6300FS, JEOL) and then are developed in a mixture of MIBK and IPA with the ratio of 1:3. Then ALD process is applied to deposit various thin films, and TiO_2 is only taken as an example here, and this technique can be extended to many other materials by ALD. The ALD process of TiO_2 is carried out in a home-built ALD system. H_2O is used as the O source, and Tetrakis (dimethylamino) titanium (TDMAT) precursor is used as a Ti source to avoid chlorine contamination and heated to 75 °C to achieve the required vapor pressure. The ALD system is under continuous 20 sccm flow of N_2 carrier gas and maintained at 105 °C throughout the process. After ALD process, a dry etching process was performed in the ICP-RIE system (Plasmalab System 100 ICP180, Oxford) with a mixed reactive gas of BCl_3 and Cl_2 to remove the TiO_2 film on the top of the resist. Finally, another dry etching process with Oxygen is applied to remove any residual resist. Scanning electron microscope (SEM) (Helios 600i, FEI) is used to characterize the morphology of the samples. The discrete distribution of the Ti, Al and Hf elements in the nanostructures are analyzed by EDX in an ultra-high resolution scanning electron microscope (Regulus 8100, Hitachi).

To fabricate the 3D hollow structures with different diameter variations, PMMA and MAA resists with the same thickness of 200 nm are spun on the substrate in sequence. Then circle patterns with diameter of 200 nm are exposed on the resist using dose of 300 μC/cm^2, followed by another exposure of circle patterns with diameter of 90 nm on the same position using dose of 700 μC/cm^2. The structures in Fig. 3f are fabricated only by changing the thickness of PMMA resist to 500 nm. Similarly, other structures are also fabricated by manipulating the order, number of layers, resist thicknesses and pattern shapes, as displayed in Fig. 3g-l.

TiO_2 hexagram nanostructure arrays with large area of 5 mm × 5 mm and the thickness of 40 nm are fabricated on quartz substrates by the ALAF method as gas sensor. Then another 10 nm TiO_2 film is deposited by ALD at 120 °C on the high aspect-ratio TiO_2 nanostructures and all other surfaces of the sample, followed by 3 nm Al_2O_3 deposition by ALD at 250 °C. The second deposition of TiO_2 can also be used to avoid defects of the as-fabricated high aspect-ratio TiO_2 nanostructures and be helpful to obtain perfect 2DEG. Then discrete Pd nanoparticles are formed uniformly on the surface of the Al_2O_3/TiO_2 heterostructure by depositing a controllable thickness of 2 nm using electron beam deposition at RT, which can be demonstrated by very high lateral resistance through the Pd nanoparticles alone. Lastly, indium is used by soldering for the bottom contact with the 2DEG, which is located at the corner of each sensor.

Numerical calculations

The phase responses and cross-polarized transmission efficiency of the metasurface are simulated by the 3D finite difference time-domain method (CST Microwave Studio). A 2D parameter sweep of a single unit with length and width from 80 nm to 150 nm and 180–300 nm, height fixed at 600 nm simultaneously, is carried out under *x*-polarization to obtain the phase map of the different structural parameters. The phase response under *y*-polarization is obtained by transposition of the *x*-polarization results. The refractive index of the TiO_2 is the measurement result by an ellipsometer. The effective refractive index is obtained from the fundamental modes while the power coupling into higher-order waveguide modes is ignored.

Optical and sensing measurements

The optical setup for vector beams manipulation from the all-dielectric metasurfaces is measured by using a supercontinuum laser source (Fianium SP 400C-PP). After passing through a linear polarizer, the linearly polarized light is focus onto the metasurface by a convex lens with focal length of 75 mm. The first order diffraction at angle of from the metasurface is analyzed by the second linear polarizer and an InGaAs infrared power meter.

Controlled amount of H_2 gas (99.999%) is introduced using a mass flow controller (MFC1), and N_2 gas (99.999%) which is injected from another mass flow controller (MFC2) to control the concentration of target gas. The mixed gas is transported in the chamber which is combined with a probe station (ST-500, Janis) with a heating chuck. The current is measured as a function of time at a fixed voltage of 3 V by a semiconductor parameter analyzer (Keithley 4200). During the measurement, the air is used for the recovery process with a relative humidity of ~50%.

CRediT authorship contribution statement

J.J. Li and G.Z. Geng conceived and designed the experiments. G.Z. Geng fabricated the samples and carried out the experiments. W.

Zhu, R.H Pan, and C.Z. Gu performed the data analysis. Z.S Zhang provided assistance for the experiment of etching process.

Declaration of Competing Interest

The authors declare that they have no known competing financial interests or personal relationships that could have appeared to influence the work reported in this paper.

Acknowledgments

Thanks to Prof. W.Y. Fu and Dr. S. Ao for the support of gas sensing experiment. This work is financially supported by the National Key R&D Program of China (Grant No. 2016YFA0200800 and 2016YFA0200400), the Natural Science Foundation of China (NSFC) (Grant Nos. 12074420, 61888102, 11674387, 61905274), the Key Research Program of Frontier Sciences of CAS (Grant No. QYZDJ-SSW-SLH042).

References

[1] M.D. Kelzenberg, S.W. Boettcher, J.A. Petykiewicz, D.B. Turner-Evans, M.C. Putnam, E.L. Warren, J.M. Spurgeon, R.M. Briggs, N.S. Lewis, H.A. Atwater, Enhanced absorption and carrier collection in Si wire arrays for photovoltaic applications, Nat. Mater. 9 (2010) 239–244, https://doi.org/10.1038/nmat2635

[2] K. Tomioka, M. Yoshimura, T. Fukui, A III–V nanowire channel on silicon for high-performance vertical transistors, Nature 488 (2012) 189–192, https://doi.org/10.1038/nature11293

[3] W. Wu, X. Wen, Z.L. Wang, Taxel-addressable matrix of vertical-nanowire piezotronic transistors for active and adaptive tactile imaging, Science 340 (2013) 952–957, https://doi.org/10.1126/science.1234855

[4] C. Pan, L. Dong, G. Zhu, S. Niu, R. Yu, Q. Yang, Y. Liu, Z.L. Wang, High-resolution electroluminescent imaging of pressure distribution using a piezoelectric nanowire LED array, Nat. Photon. 7 (2013) 752–758, https://doi.org/10.1038/nphoton.2013.191

[5] P. Banerjee, I. Perez, L. Henn-Lecordier, S.B. Lee, G.W. Rubloff, Nanotubular metal–insulator–metal capacitor arrays for energy storage, Nat. Nanotechnol. 4 (2009) 292–296, https://doi.org/10.1038/nnano.2009.37

[6] C. Liu, E.I. Gillette, X. Chen, A.J. Pearse, A.C. Kozen, M.A. Schroeder, K.E. Gregorczyk, S.B. Lee, G.W. Rubloff, An all-in-one nanopore battery array, Nat. Nanotechnol. 9 (2014) 1031–1039, https://doi.org/10.1038/nnano.2014.247

[7] M. Najiminaini, E. Ertorer, B. Kaminska, S. Mittler, J.J.L. Carson, Surface plasmon resonance sensing properties of a 3D nanostructure consisting of aligned nanohole and nanocone arrays, Analyst 139 (2014) 1876–1882, https://doi.org/10.1039/C3AN02332J

[8] N. Liu, M.L. Tang, M. Hentschel, H. Giessen, A.P. Alivisatos, Nanoantenna-enhanced gas sensing in a single tailored nanofocus, Nat. Mater. 10 (2011) 631–636, https://doi.org/10.1038/nmat3029

[9] T. Jain, M. Aernecke, V. Liberman, R. Karnik, High resolution fabrication of nanostructures using controlled proximity nanostencil lithography, Appl. Phys. Lett. 104 (2014) 083117, https://doi.org/10.1063/1.4867014

[10] X. Fu, P. Li, A.Z. Jin, H.Y. Zhang, H. Yang, Gas-assisted focused ion beam etching characteristics of niobium, J. Vac. Sci. Technol. B 23 (2005) 585–587, https://doi.org/10.1116/1.1884121

[11] D. Gu, H. Baumgart, T.M. Abdel-Fattah, G. Namkoong, Synthesis of nested coaxial multiple-walled nanotubes by atomic layer deposition, ACS Nano 4 (2010) 753–758, https://doi.org/10.1021/nn901250w

[12] L. Wen, R. Xu, Y. Mi, Y. Lei, Multiple nanostructures based on anodized aluminium oxide templates, Nat. Nanotechnol. 12 (2017) 244–250, https://doi.org/10.1038/nnano.2016.257

[13] W. Li, D. Kuang, P. Gu, M. Xiang, Partially disordered TiO_2 nanotube photonic crystal: randomness characterization and tuning of reflected scattering light, Nanotechnology 31 (2019) 025711, https://doi.org/10.1088/1361-6528/ab483b

[14] D.O. Shin, J.H. Mun, G.-T. Hwang, J.M. Yoon, J.Y. Kim, J.M. Yun, Y.-B. Yang, Y. Oh, J.Y. Lee, J. Shin, K.J. Lee, S. Park, J.U. Kim, S.O. Kim, Multicomponent nanopatterns by directed block copolymer self-assembly, ACS Nano 7 (2013) 8899–8907, https://doi.org/10.1021/nn403379k

[15] D. Men, Y. Wu, C. Wang, J. Xiang, G. Yang, C. Wan, H. Zhang, Wafer-scale hierarchical nanopillar arrays based on au masks and reactive ion etching for effective 3D SERS substrate, Materials 11 (2018) 239, https://doi.org/10.3390/ma11020239

[16] X. Meng, X. Wang, D. Geng, C. Ozgit-Akgun, N. Schneider, J.W. Elam, Atomic layer deposition for nanomaterial synthesis and functionalization in energy technology, Mater. Horiz. 4 (2017) 133–154, https://doi.org/10.1039/C6MH00521G

[17] Z. Zhao, Y. Kong, Z. Zhang, G. Huang, Y. Mei, Atomic layer–deposited nanostructures and their applications in energy storage and sensing, J. Mater. Res. 35 (2020) (2020) 701–719, https://doi.org/10.1557/jmr.2019.329

[18] F. Naeem, S. Naeem, Y. Zhao, D. Wang, J. Zhang, Y. Mei, G. Huang, TiO_2 nanomembranes fabricated by atomic layer deposition for supercapacitor electrode with enhanced capacitance, Nanoscale Res. Lett. 14 (2019) 92, https://doi.org/10.1186/s11671-019-2912-3

[19] R.E. Rodríguez, S.P. Agarwal, S. An, E. Kazyak, D. Das, W. Shang, R. Skye, T. Deng, N.P. Dasgupta, Biotemplated morpho butterfly wings for tunable structurally colored photocatalysts, ACS Appl. Mater. Interfaces 10 (2018) 4614–4621, https://doi.org/10.1021/acsami.7b14383

[20] F. Xiao, J. Miao, H. Tao, S.-F. Hung, H.Y. Wang, H. Yang, J. Chen, R. Chen, B. Liu, One-dimensional hybrid nanostructures for heterogeneous photocatalysis and photoelectrocatalysis, Small 11 (2015) 2115–2131, https://doi.org/10.1002/smll.201402420

[21] L. Wen, Z. Wang, Y. Mi, R. Xu, S.-H. Yu, Y. Lei, Designing heterogeneous 1D nanostructure arrays based on AAO templates for energy applications, Small 11 (2015) 3408–3428, https://doi.org/10.1002/smll.201500120

[22] D. Gu, H. Baumgart, K. Tapily, P. Shrestha, G. Namkoong, X. Ao, F. Müller, Precise control of highly ordered arrays of nested semiconductor/metal nanotubes, Nano Res. 4 (2011) 164–170, https://doi.org/10.1007/s12274-010-0066-9

[23] E. Shkondin, H. Alimadadi, O. Takayama, F. Jensen, A.V. Lavrinenko, Fabrication of hollow coaxial $Al_2O_3/ZnAl_2O_4$ high aspect ratio freestanding nanotubes based on the Kirkendall effect, J. Vac. Sci. Technol. A 38 (2020) 013402, https://doi.org/10.1116/1.5130176

[24] Y. Luo, S.K. Lee, H. Hofmeister, M. Steinhart, U. Gösele, Pt nanoshell tubes by template wetting, Nano Lett. 4 (2004) 143–147, https://doi.org/10.1021/nl034897k

[25] L. Wen, R. Xu, C. Cui, W. Tang, Y. Mi, X. Lu, Z. Zeng, S.L. Suib, P.-X. Gao, Y. Lei, Template-guided programmable janus heteronanostructure arrays for efficient plasmonic photocatalysis, Nano Lett. 18 (2018) 4914–4921, https://doi.org/10.1021/acs.nanolett.8b01675

[26] T. Tynell, M. Karppinen, Atomic layer deposition of ZnO: a review, Semicond. Sci. Technol. 29 (2014) 043001, https://doi.org/10.1088/0268-1242/29/4/043001

[27] Z. Zhou, S.S. Nonnenmann, Progress in nanoporous templates: beyond anodic aluminum oxide and towards functional complex materials, Materials 12 (2019) 2535, https://doi.org/10.3390/ma12162535

[28] Y.-H. Chang, C.-M. Liu, Y.-C. Tseng, C. Chen, C.-C. Chen, H.-E. Cheng, Direct probe of heterojunction effects upon photoconductive properties of TiO_2 nanotubes fabricated by atomic layer deposition, Nanotechnology 21 (2010) 225602, https://doi.org/10.1088/0957-4484/21/22/225602

[29] J. Bachmann, Jing, M. Knez, S. Barth, H. Shen, S. Mathur, U. Gösele, K. Nielsch, Ordered iron oxide nanotube arrays of controlled geometry and tunable magnetism by atomic layer deposition, J. Am. Chem. Soc. 129 (2007) 9554–9555, https://doi.org/10.1021/ja072465w

[30] Z. Wan, H.J. Lee, H.G. Kim, G.C. Jo, W.I. Park, S.W. Ryu, H.-B.-R. Lee, S.-H. Kwon, Circular double-patterning lithography using a block copolymer template and atomic layer deposition, Adv. Mater. Interfaces 5 (2018) 1800054, https://doi.org/10.1002/admi.201800054

[31] J. Li, W. Liu, J. Wang, I. Rozen, S. He, C. Chen, H.G. Kim, H.-J. Lee, H.-B.-R. Lee, S.-H. Kwon, T. Li, L. Li, J. Wang, Y. Mei, Nanoconfined atomic layer deposition of TiO_2/Pt nanotubes: toward ultrasmall highly efficient catalytic nanorockets, Adv. Funct. Mater. 27 (2017) 1700598, https://doi.org/10.1002/adfm.201700598

[32] S. Peng, R. Zhang, V.H. Chen, E.T. Khabiboulline, P. Braun, H.A. Atwater, Three-dimensional single gyroid photonic crystals with a mid-infrared bandgap, ACS Photonics 3 (2016) 1131–1137, https://doi.org/10.1021/acsphotonics.6b00293

[33] L.R. Meza, J.R. Greer, Mechanical characterization of hollow ceramic nanolattices, J. Mater. Sci. 49 (2014) 2496–2508, https://doi.org/10.1007/s10853-013-7945-x

[34] C. Ahn, S.-M. Kim, J.-W. Jung, J. Park, T. Kim, S.E. Lee, D. Jang, J.-W. Hong, S.M. Han, S. Jeon, Multifunctional polymer nanocomposites reinforced by 3D continuous ceramic nanofillers, ACS Nano 12 (2018) 9126–9133, https://doi.org/10.1021/acsnano.8b03264

[35] Y.-e Na, D. Shin, K. Kim, C. Ahn, S. Jeon, D. Jang, Emergence of new density-strength scaling law in 3D hollow ceramic nanoarchitectures, Small 14 (2018) 1802239, https://doi.org/10.1002/smll.201802239

[36] K. Kim, J. Park, S. Hong, S.H. Park, S.G. Jeon, C. Ahn, J.Y. Song, S. Jeon, Anomalous thermoelectricity of pure ZnO from 3D continuous ultrathin nanoshell structures, Nanoscale 10 (2018) 3046–3052, https://doi.org/10.1039/C7NR08167G

[37] P. Birnal, M.C. Marco de Lucas, I. Pochard, B. Domenichini, L. Imhoff, Photocatalytic properties of atomic layer deposited TiO_2 inverse opals and planar films for the degradation of dyes, Appl. Surf. Sci. 512 (2020) 145693, https://doi.org/10.1016/j.apsusc.2020.145693

[38] J. Long, M. Fu, C. Li, C. Sun, D. He, Y. Wang, High-quality ZnO inverse opals and related heterostructures as photocatalysts produced by atomic layer deposition, Appl. Surf. Sci. 454 (2018) 112–120, https://doi.org/10.1016/j.apsusc.2018.05.160

[39] M. Seo, S. Yoon, H. Cho, S. Lee, K. Kim, B.D. Kong, M. Meyyappan, C. Baek, Solar cell using hourglass-shaped silicon nanowires for increased light-trapping path, IEEE J. Photovolt. 10 (2020) 475–479, https://doi.org/10.1109/JPHOTOV.2020.2964329

[40] G.D. Sulka, A. Brzózka, L. Liu, Fabrication of diameter-modulated and ultrathin porous nanowires in anodic aluminum oxide templates, Electrochim. Acta 56 (2011) 4972–4979, https://doi.org/10.1016/j.electacta.2011.03.126

[41] B. Hua, B. Wang, M. Yu, P.W. Leu, Z. Fan, Rational geometrical design of multi-diameter nanopillars for efficient light harvesting, Nano Energy 2 (2013) 951–957, https://doi.org/10.1016/j.nanoen.2013.03.016

[42] N.K. Grady, J.E. Heyes, D.R. Chowdhury, Y. Zeng, M.T. Reiten, A.K. Azad, A.J. Taylor, D.A.R. Dalvit, H.-T. Chen, Terahertz metamaterials for linear polarization conversion and anomalous refraction, Science 340 (2013) 1304–1307, https://doi.org/10.1126/science.1235399

[43] J. Valentine, S. Zhang, T. Zentgraf, E. Ulin-Avila, D.A. Genov, G. Bartal, X. Zhang, Three-dimensional optical metamaterial with a negative refractive index, Nature 455 (2008) 376–379, https://doi.org/10.1038/nature07247

[44] T. Ergin, N. Stenger, P. Brenner, J.B. Pendry, M. Wegener, Three-dimensional invisibility cloak at optical wavelengths, Science 328 (2010) 337–339, https://doi.org/10.1126/science.1186351
[45] L. Zhang, S. Liu, L. Li, T. Cui, Spin-controlled multiple pencil beams and vortex beams with different polarizations generated by pancharatnam-berry coding metasurfaces, ACS Appl. Mater. Interfaces 9 (2017) 36447–36455, https://doi.org/10.1021/acsami.7b12468
[46] Y. Liu, Y. Ke, J. Zhou, Y. Liu, H. Luo, S. Wen, D. Fan, Generation of perfect vortex and vector beams based on Pancharatnam-Berry phase elements, Sci. Rep. 7 (2017) 44096, https://doi.org/10.1038/srep44096
[47] W. Luo, S. Sun, H.-X. Xu, Q. He, L. Zhou, Transmissive ultrathin pancharatnam-berry metasurfaces with nearly 100% efficiency, Phys. Rev. Appl. 7 (2017) 044033, https://doi.org/10.1103/PhysRevApplied.7.044033
[48] S. Kim, H. Kim, H. Jung, J.-Y. Park, T. Seok, Y.-H. Choa, T.J. Park, S. Lee, High-performance, transparent thin film hydrogen gas sensor using 2D electron gas at interface of oxide thin film heterostructure grown by atomic layer deposition, Adv. Funct. Mater. 29 (2018) 1807760, https://doi.org/10.1002/adfm.201807760
[49] T.J. Seok, Y. Liu, H.J. Jung, S.B. Kim, D.H. Kim, S.M. Kim, J.H. Jang, D.-Y. Cho, S.W. Lee, T.J. Park, Field-effect device using quasi-two-dimensional electron gas in mass-producible atomic-layer-deposited Al_2O_3/TiO_2 ultrathin (<10 nm) film heterostructures, ACS Nano 12 (2018) 10403–10409, https://doi.org/10.1021/acsnano.8b05891
[50] K. Yoshimura, C. Langhammer, B. Dam, Metal hydrides for smart window and sensor applications, MRS Bull. 38 (2013) 495–503, https://doi.org/10.1557/mrs.2013.129
[51] H. Gu, Z. Wang, Y. Hu, Hydrogen gas sensors based on semiconductor oxide nanostructures, Sensors 12 (2012) 5517–5550, https://doi.org/10.3390/s120505517
[52] N.Y. Chan, M. Zhao, J. Huang, K. Au, M.H. Wong, H.M. Yao, W. Lu, Y. Chen, C.W. Ong, H.L.W. Chan, J. Dai, Highly sensitive gas sensor by the $LaAlO_3/SrTiO_3$ heterostructure with Pd nanoparticle surface modulation, Adv. Mater. 26 (2014) 5962–5968, https://doi.org/10.1002/adma.201401597
[53] W.T. Koo, S. Qiao, A.F. Ogata, G. Jha, J.S. Jang, V.T. Chen, I.D. Kim, R.M. Penner, Accelerating palladium nanowire H_2 sensors using engineered nanofiltration, ACS Nano 11 (2017) 9276–9285, https://doi.org/10.1021/acsnano.7b04529
[54] Y.T. Cheng, Y. Li, D. Lisi, W.M. Wang, Preparation and characterization of Pd/Ni thin films for hydrogen sensing, Sens. Actuators B Chem. 30 (1996) 11–16, https://doi.org/10.1016/0925-4005(95)01734-D